

## SPECIAL ISSUE ARTICLE

# In situ studies on temperature-dependent deformation mechanisms of Al<sub>2</sub>O<sub>3</sub> prepared by spark plasma sintering

Chao Shen<sup>1</sup>  | Tongjun Niu<sup>1</sup> | Jaehun Cho<sup>1,3</sup> | Tianyi Sun<sup>1</sup> | Anyu Shang<sup>1</sup> |  
Yifan Zhang<sup>1</sup> | Haiyan Wang<sup>1,2</sup>  | Xinghang Zhang<sup>1</sup> 

<sup>1</sup>School of Materials Engineering, Purdue University, West Lafayette, Indiana, USA

<sup>2</sup>School of Electrical and Computer Engineering, Purdue University, West Lafayette, Indiana, USA

<sup>3</sup>School of Materials Science and Engineering, Kumoh National Institute of Technology, Gumi, Republic of Korea

## Correspondence

Chao Shen and Xinghang Zhang, School of Materials Engineering, Purdue University, West Lafayette, IN 47907, USA.  
Email: [xzhang98@purdue.edu](mailto:xzhang98@purdue.edu); [shen569@purdue.edu](mailto:shen569@purdue.edu)

## Funding information

Office of Naval Research, Grant/Award Numbers: N00014-17-1-2087, N00014-22-1-2160, N00014-20-1-2043, N00014-20-1-2659

## Abstract

Alumina ( $\alpha$ -Al<sub>2</sub>O<sub>3</sub>) is one of the most versatile engineering ceramics, and its mechanical properties have been extensively studied. However, the micromechanical properties of Al<sub>2</sub>O<sub>3</sub> with a fine microstructure are less well understood. Here, we present one of the first investigations that probe the micromechanical properties of fine-grained polycrystalline Al<sub>2</sub>O<sub>3</sub> fabricated via spark plasma sintering, employing in situ microcompression tests inside a scanning electron microscope. This study explores the influence of temperature variations on the deformation mechanisms, particularly the involvement of microcracks and dislocation activities throughout the deformation process. As temperature rises, substantial deformability occurs in the inherently brittle Al<sub>2</sub>O<sub>3</sub> at intermediate temperature, where the improved plastic deformability mainly arose from prominent dislocation activities accompanied by grain boundary sliding. This study sheds light on understanding the relationship between defect evolution and mechanical behavior in Al<sub>2</sub>O<sub>3</sub> with fine grain sizes.

## KEYWORDS

Al<sub>2</sub>O<sub>3</sub>, in-situ microcompression test, plasticity, transmission electron microscopy

## 1 | INTRODUCTION

Alumina ( $\alpha$ -Al<sub>2</sub>O<sub>3</sub>) is one of the representative ceramic materials used in critical structural components due to its superior hardness and strength-to-weight ratio.<sup>1–4</sup> Processing of Al<sub>2</sub>O<sub>3</sub> by a conventional pressureless consolidation method takes more than 10 hours above 1400°C to reach a high relative density.<sup>5</sup> As the high temperature and long sintering time lead to significant grain coarsening, an alternative sintering technique is necessary to prepare dense specimens with desired fine microstructures.<sup>6</sup> Spark plasma sintering (SPS) is an efficient method that

enables the densification of ceramic and metal powders at low temperatures with a short holding time.<sup>7–10</sup> By applying an electric field, a high current will flow through the conductive tooling. The resulting Joule heating can provide high heating rates that alleviate grain coarsening, and contribute to the densification of powders at low temperatures.<sup>6,11</sup> Although there have been arguments on whether the electric discharge at spaces between powders can be generated during SPS, the plasma may enhance densification through effectively purging adsorbed gases adhering to the surface of particles.<sup>12–14</sup> The impact of spark discharges on densification is most significant

This is an open access article under the terms of the [Creative Commons Attribution](https://creativecommons.org/licenses/by/4.0/) License, which permits use, distribution and reproduction in any medium, provided the original work is properly cited.

© 2024 The Author(s). *Journal of the American Ceramic Society* published by Wiley Periodicals LLC on behalf of American Ceramic Society.

during the initial stages of sintering, as numerous gaps between particles facilitate the generation of spark discharges.<sup>15</sup> However, once the sample achieves a state of closed porosity, densification is predominantly driven by grain boundary and lattice diffusion mechanisms.<sup>15</sup>

There have been many attempts to fabricate the dense and fine Al<sub>2</sub>O<sub>3</sub> by means of a wide range of heating rates and pressures through the SPS technique.<sup>16–20</sup> In a study by Shen et al., the influence of heating rate on the densification and grain growth of Al<sub>2</sub>O<sub>3</sub> during SPS was investigated across a range of 50–600°C/min.<sup>16</sup> A heating rate of ≤ 350°C/min resulted in fully dense Al<sub>2</sub>O<sub>3</sub>, while higher heating rates led to the formation of a porous structure.<sup>16</sup> Meanwhile, Zhou et al. demonstrated that the densification and grain growth behaviors of Al<sub>2</sub>O<sub>3</sub> exhibit significant variation depending on the applied heating rates. A fast heating rate can substantially enhance the formation of necking between particles at the early stage of sintering and ultimately result in higher densities and smaller grain sizes compared to a slower heating rate.<sup>18</sup> On the other hand, Ratzker et al. showed that full densification of alumina via the SPS technique could be attained at 1050°C by employing high pressures ranging from 500 to 800 MPa.<sup>20</sup> However, the application of the high pressure led to significant dynamic grain growth facilitated by grain boundary sliding, grain rotation, and coalescence.<sup>20</sup>

The wide application of Al<sub>2</sub>O<sub>3</sub> as a structural material requires a thorough understanding of its mechanical performance over a broad temperature range. However, the deformation mechanisms in Al<sub>2</sub>O<sub>3</sub> are difficult to examine due to its brittle behavior and high mechanical strength.<sup>21</sup> Prior research on the mechanical properties of single-crystal (SC) Al<sub>2</sub>O<sub>3</sub> discloses a wide range of deformation mechanisms including cracks, twinning, and dislocations.<sup>21–28</sup> It is reported that SCs oriented along  $\langle 1\bar{2}10 \rangle$  are more prone to plastic flow than other orientations under room temperature (RT) deformation.<sup>21</sup> On the other hand, deformation twinning carries the majority of the plastic strain apart from dislocation when the SC Al<sub>2</sub>O<sub>3</sub> is oriented for the basal slip near 200°C.<sup>24</sup> Furthermore, some studies on the polycrystalline Al<sub>2</sub>O<sub>3</sub> by bend test demonstrated that specimens with a fine grain size exhibited deformability at temperatures as high as 1500°C, with a brittle-ductile transition temperature of 1350°C.<sup>29–31</sup> Three deformation mechanisms may take place at elevated temperatures, including diffusional creep, basal slip, and grain boundary sliding. While most SC and polycrystalline ceramics are brittle, and susceptible to crack nucleation and propagation at RT, plasticity emerges when the temperature increases beyond the brittle-to-ductile transition temperature (BDTT).<sup>29</sup> Strategies involving a hydrostatic pressure or reducing the sample dimension can reduce the BDTT.<sup>21,32</sup> Therefore,

in situ micropillar compression offers the opportunity to investigate the temperature-dependent deformation mechanisms of brittle materials at elevated temperatures by controlling the specimen volume at the microscale.<sup>33–35</sup> Furthermore, while some previous studies focused on SC Al<sub>2</sub>O<sub>3</sub> using compression testing, the bend test is commonly utilized in studies involving polycrystalline Al<sub>2</sub>O<sub>3</sub>, and there is limited research on polycrystalline Al<sub>2</sub>O<sub>3</sub> under uniaxial compression. The non-uniform stress distribution induced by the bending moment complicates the accurate interpretation of the stress-strain relationship in the bend test. In contrast, uniaxial compression offers a direct assessment of compressive properties such as compressive strength, modulus of elasticity, and deformation behavior under compression. This method provides valuable insights into the material's response to compressive loading conditions, contributing to a more comprehensive understanding of its mechanical behavior.

Here, we report an in situ micropillar compression study on the mechanical response of SPS Al<sub>2</sub>O<sub>3</sub> with an average grain size of 420 nm at elevated temperatures (up to 740°C). The temperature-dependent transition of deformation mechanisms was observed. Furthermore, the in situ studies highlighted the reduced BDTT for fine-grained Al<sub>2</sub>O<sub>3</sub> compared to previous studies of deformation behaviors at macroscales.

## 2 | EXPERIMENTAL METHODS

### 2.1 | Specimen preparation

High purity  $\alpha$ -Al<sub>2</sub>O<sub>3</sub> powder (US Research Nanomaterials, Inc., 99.9%, 135 nm particle size) was sintered by the SPS technique. The powder was placed in a cylindrical graphite die with an inner diameter of 10 mm. A graphite foil was inserted into the inner wall to prevent the powder from adhering to the graphite tooling. The SPS system (SPS-10; Thermal Technologies LLC) was powered on when the vacuum in the chamber reached  $2 \times 10^{-2}$  torr. The sintering temperature ramped to 1200°C at a heating rate of 200°C/min and held for 10 mins along with a pressure of 60 MPa. The relative density of the sintered specimen was measured to be higher than 99% by the Archimedes method.

### 2.2 | Microstructure characterizations

The structure of SPS Al<sub>2</sub>O<sub>3</sub> was characterized by the X-ray diffraction (XRD) technique by using a PANalytical Empyrean X'pert PRO MRD diffractometer with a  $2 \times \text{Ge} (220)$  hybrid monochromator to select Cu K $\alpha_1$  in

the  $2\theta-\omega$  geometrical configuration. A Thermo Fisher Quanta 650 FEG scanning electron microscope (SEM) and an FEI Talos 200X transmission electron microscope (TEM) operated at 200 kV were utilized to analyze the microstructure of specimens. Grain sizes were estimated by the line intercept method over 200 grains based on TEM images. TEM samples were manually prepared by grinding, polishing, dimpling and final polishing in an Ar ion milling system (PIPS ii, Gatan) at 2 kV. The crystallographic information embedded in the Inverse pole figure (IPF) and Kernel average misorientation (KAM) maps were generated by procession electron diffraction equipment (ASTAR; NanoMEGAS) installed in the FEI Talos 200X TEM microscope.

### 2.3 | In situ micropillar compression testing

The SPS  $\text{Al}_2\text{O}_3$  was manually polished on diamond papers (15–1  $\mu\text{m}$ ) and colloidal silica (20 nm) to minimize the surface roughness. The polished samples were mounted on a specimen stub to coat a thin layer of platinum at 40 mA for 60 seconds to enhance the electric conductivity in SEM. Micropillars with  $\sim 3 \mu\text{m}$  in diameter and 6  $\mu\text{m}$  in height (an aspect ratio of diameter to height of  $\sim 1:2$ ) were fabricated using a focused ion beam in a Thermofisher Quanta 3D FEG scanning electron microscope. A series of decelerated currents (from 30–0.3 nA) was used to fabricate the pillars in the center of a large crater, with a smooth surface and minimized tapering angle. A Hysitron PI 88  $\times$  R PicoIndenter equipped with a piezoelectric actuator on the capacitive transducer was installed in a Quanta 3D FEG microscope to perform in situ SEM micropillar compression tests. A 20- $\mu\text{m}$  diameter diamond flat punch was mounted on the transducer to collect force-displacement data during compression. The specimen was tightly fixed by a V-shape Mo clamp on a ceramic heating stage to maximize the heat transfer and minimize machine compliance. The temperature on both the heating stage and probe heater was ramped up simultaneously at a rate of  $10^\circ\text{C}/\text{min}$  and isothermally stabilized for 30 min to eliminate thermal drift. An average drift rate of less than 0.7 nm/s was monitored in the preloading process at each testing temperature. Each mechanical test was performed at a strain rate of  $5 \times 10^{-3} \text{ s}^{-1}$  under displacement control mode.

## 3 | RESULTS

Detailed characterization was performed on as-sintered SPS  $\text{Al}_2\text{O}_3$  before the in situ compression test. XRD study in Figure S1 confirms the existence of  $\alpha\text{-Al}_2\text{O}_3$ , where

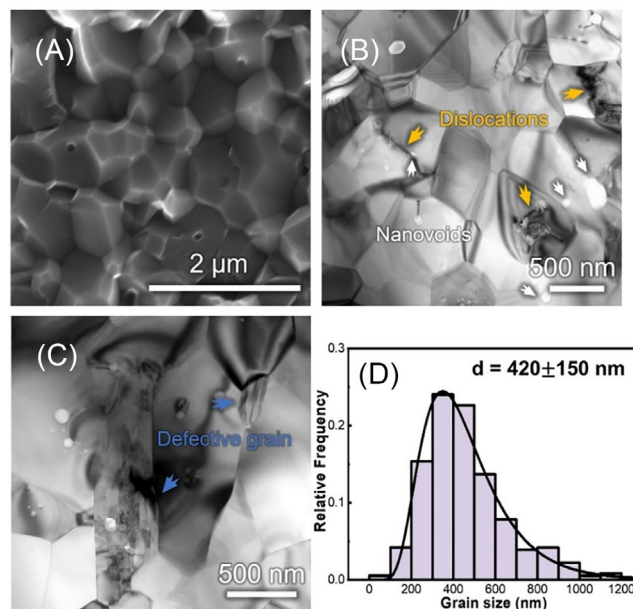


**FIGURE 1** Characterization of the grain morphology and grain size distribution of the spark plasma sintering (SPS)  $\text{Al}_2\text{O}_3$ . (A) Scanning electron microscopy (SEM) micrograph of the SPS  $\text{Al}_2\text{O}_3$  showing typical granular morphology. (B) Bright-field (BF) transmission electron microscopy (TEM) image shows dislocations (orange arrows) and nanovoids (white arrows) formed in the specimen. (C) BF TEM image shows some defective grains (blue arrows). (D) Statistics of grain size distribution show an average grain size of 420 nm.

no phase transformation occurred in the polycrystal specimen. Figure 1 exhibits the morphology and statistics of the grains of  $\text{Al}_2\text{O}_3$  with a relative density of more than 99% after SPS. The SEM image in Figure 1A shows the typical equiaxed granular morphology. Bright-field (BF) TEM images in Figure 1B,C display the existence of nanovoids, dislocations, and defective grains decorated with a high density of stacking faults (SFs). A zoom-in TEM micrograph of a defective grain is provided in Figure S2. Numerous SFs were observed within the defective grains. The average grain size is 420 nm according to the statistical distribution in Figure 1D. Microindentation tests were performed on the well-polished surface of the specimen at a load of 1 kg with a Vickers tip to measure the hardness and indentation fracture toughness. Figure S3 shows the representative indentation morphology, and the cracks near the indented corner were highlighted by dashed lines. The Vickers hardness was calculated to be  $14.1 \pm 0.9 \text{ GPa}$  with the indentation fracture toughness of  $3.48 \pm 0.11 \text{ MPa} \cdot \sqrt{\text{m}}$  from the following equation,<sup>36</sup>

$$K_{Ic} = 0.0154 \cdot \left( \frac{E}{HV} \right)^{\frac{1}{2}} \cdot \left( \frac{P}{c^2} \right) \quad (1)$$

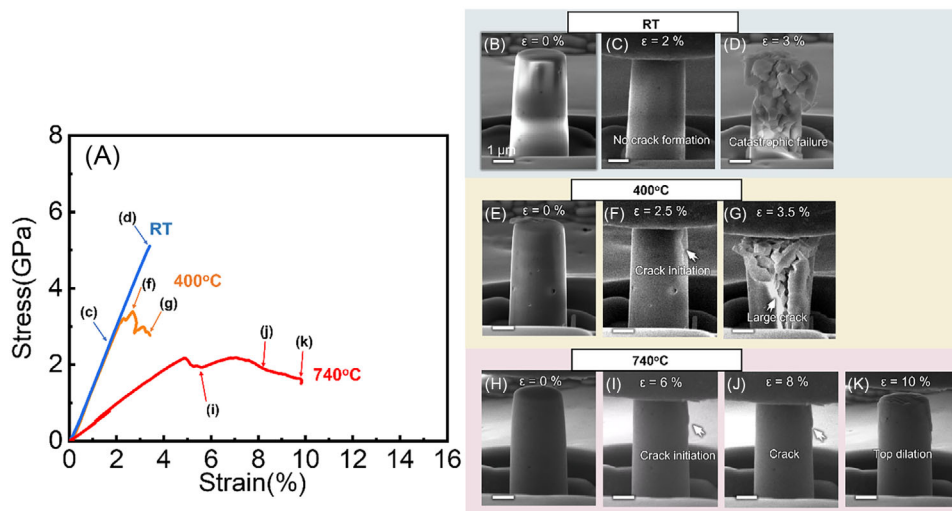


**FIGURE 2** Comparison of true stress-strain behaviors and the morphology evolution on the spark plasma sintering (SPS)  $\text{Al}_2\text{O}_3$  under uniaxial in situ microcompression tests at room temperature (RT), 400°C, and 740°C at a constant strain rate of  $5 \times 10^{-3} \text{ s}^{-1}$ . (A) Comparison of stress-strain curves for specimens tested at various temperatures. (B–D) At RT, the micropillar experienced catastrophic failure at 3% strain right after the crack nucleation, and it broke into halves. (E–G) For micropillars tested at 400°C, cracks were initiated at 2.5% strain. Giant longitudinal cracks propagated downward throughout the entire pillar at 3.5% strain. (H–K) At 740°C, the crack initiated at 6% strain. The pillar gradually deformed to 10% strain. A dilated top and some intergranular cracks were observed. See Video S1–S3 for details.

where  $K_{IC}$  is the indentation fracture toughness,  $E$  is the elastic modulus,  $HV$  is the Vickers hardness,  $P$  is the applied load, and  $c$  is the crack length from the indent center.

Numerous micropillars on the SPS  $\text{Al}_2\text{O}_3$  were compressed at RT, 400, and 740°C, and the results showed good reproducibility as shown in Figure S4. All deformation experiments were conducted at the same strain rate of  $5 \times 10^{-3} \text{ s}^{-1}$ . Stress-strain curves along with the SEM snapshots of compressed pillars at different strain levels are shown in Figure 2. During the deformation under RT, all pillars experienced brittle failure at a strain of 3% or less at high flow stress of nearly 5 GPa. The catastrophic failure occurred when half of the pillar was chucked off immediately upon the crack nucleation as shown in Figure 2D. On the other hand, when tested at 400°C, cracks nucleated at 2.5% strain and the maximum stress reached 3.5 GPa. Several cracks propagated downwards slowly and converged into a large vertical crack as labeled in Figure 2G. When the pillar failed at 3.5% strain, an outward buckling occurred in the top portion of the deformed pillar. At 740°C, significantly enhanced deformability was observed. The crack nucleated when  $\varepsilon = 6\%$  at a stress of 2 GPa, after which plastic flow with a stress plateau was observed upon successive compression. At 10% strain, dilation appeared in the pillar top together with some shear offset caused by cracks. See Video S1–S3 for details.

The fracture morphology of micropillars after compression under various temperatures was examined by SEM at different viewing angles (top-down and side-view). As

shown in Figure 3A,B, a brittle fracture was detected in the deformed pillar after RT compression, where subgrains formed near the pillar top by transgranular cracking. In comparison, intergranular cracking dominated in the pillar tested at 400°C, and the grain morphology in the pillar interior was revealed by the large longitudinal crack. For pillars tested at 740°C, no prominent crack opening was detected. Some microcracks propagated along the grain boundaries (GBs) on the peripheral surface as shown in Figure 3E,F.

To investigate the microstructure and defect evolution after mechanical tests over a broad temperature range, post-mortem TEM analyses were performed on pillars deformed under three conditions. In the case of pillars tested at RT, only half of the pillar survived at 3% strain upon catastrophic failure. Meanwhile, grain fragmentation was commonly observed near the pillar top, as shown in Figure 4A. A few SFs were observed in the deformed region (Figure 4B). No grain rotation or sliding was observed in the IPF map in Figure 4C. The KAM map and the geometrically necessary dislocation (GND) map indicate insignificant misorientation angles and few dislocation activities (as shown in Figure 4D,E) in the deformed pillar.

In comparison, for the pillar tested at 400°C, two inclined cracks transmitted from the pillar top, and then converged into one giant intergranular crack propagating downwards through the entire pillar, as displayed in Figure 5A. It is interesting to note that one crack was deflected by an elongated grain as shown in Figure 5B.

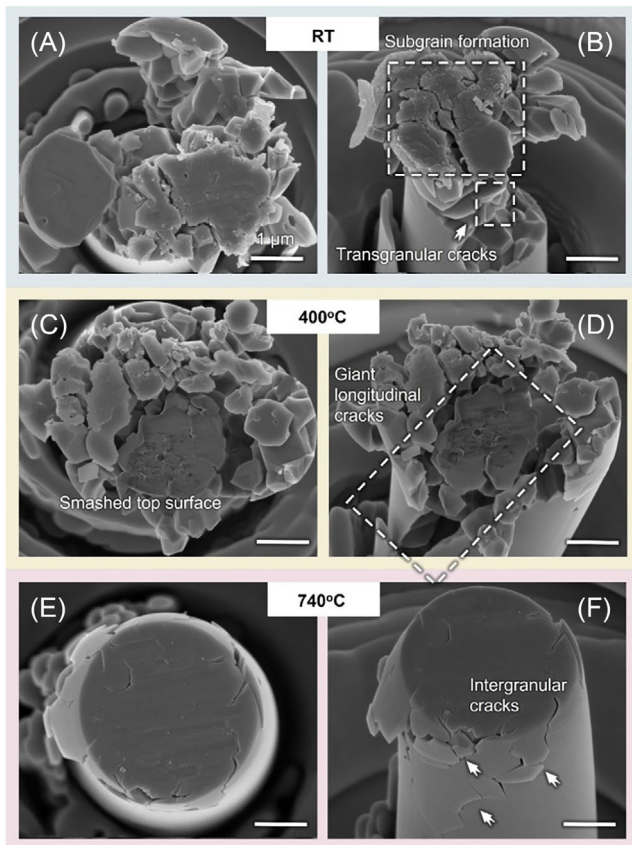


**FIGURE 3** The scanning electron microscopy (SEM) images show the top and side views of deformed micropillars tested at room temperature (RT), 400°C, and 740°C. (A, B) For the remaining portion of the micropillar tested at RT, transgranular fracture was evident on the top in which subgrains formed. (C, D) For micropillar tested at 400°C, the top half was smashed by transgranular fracture, and the giant longitudinal cracks propagated downwards intergranularly throughout the entire pillar. (E, F) At 740°C, some microcracks were observed from the top area. Intergranular cracks propagated along grain boundaries as observed on the side surface.

The high-resolution TEM image in Figure 5C illustrates the formation of a curved low-angle grain boundary ( $10^\circ$ ) to accommodate the plastic strain. The IPF and KAM map in Figure 5D,E indicate that the intergranular cracks dominate. A high degree of misorientation was observed near cracks. The GND map in Figure 5F correlates well with the KAM map showing limited dislocation activities.

Enhanced deformability was observed in the pillar deformed at 740°C as shown in Figure 6A. A high density of dislocations was generated in the deformed top region (Figure 6B), while the bottom half of the grain interior is relatively clean with fewer defects (Figure 6C). In addition, the IPF map in Figure 6B shows that grain morphology has changed from the equiaxed to an

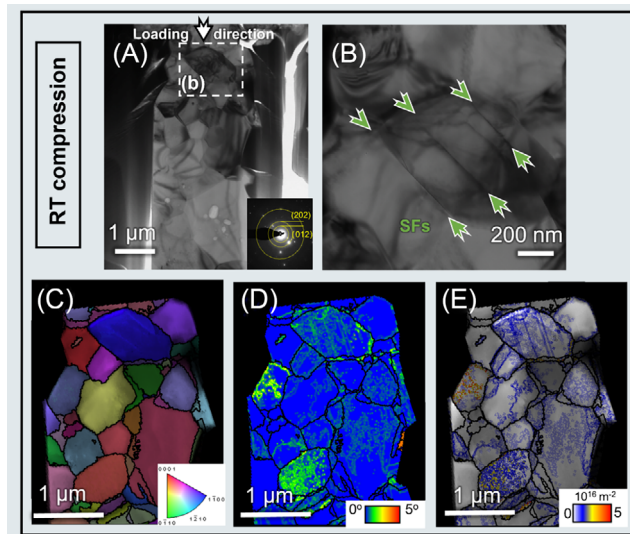


**FIGURE 4** The post-mortem transmission electron microscopy (TEM) analyses of the spark plasma sintering (SPS)  $\text{Al}_2\text{O}_3$  micropillar after room temperature (RT) compression. (A) A bright-field (BF) TEM micrograph showing a half of the micropillar survived after being deformed to 3% strain. (B) Some stacking faults (SFs) were observed within the grain in the micropillar. (C) An inverse pole figure (IPF) map of the fractured micropillar confirmed no grain rotation in the polycrystalline pillar. (D) The kernel average misorientation (KAM) map indicates few degrees of misorientation and fewer dislocation activities in the remaining portion of the fractured pillar. (E) The geometrically necessary dislocation (GND) map shows a few grains with GND distribution.

elongated shape in the top region, while grains in the bottom half of the pillar remain equiaxed, indicating that plastic deformation was primarily accommodated by the top region. The KAM map in Figure 6E exhibits some gaps (grain separation) near the pillar top, which originated from a large extent of grain boundary sliding, as shown in Figure 6D. The KAM map in Figure 6E exhibits a high degree of intragranular misorientations in the elongated grains and such misorientation was also observed in the lower portion of the deformed pillar. The GND map shows evident dislocations in the deformed micropillar.

Figure 7A shows the evolution of the KAM value as a function of test temperature. Below 400°C, the KAM value of the deformed region is similar to the undeformed region, while it increases evidently when the test temperature reaches 740°C. Figure 7B,C illustrates the evolution of maximum flow stress with test temperature, alongside the literature data on the compressive strength of SC and polycrystalline  $\text{Al}_2\text{O}_3$ .<sup>23,24,37,38</sup> It is evident that the maximum flow stress of polycrystalline  $\text{Al}_2\text{O}_3$  is comparable to that of SC  $\text{Al}_2\text{O}_3$  at elevated temperatures (even surpassing it slightly when tested at 740°C), and decreases

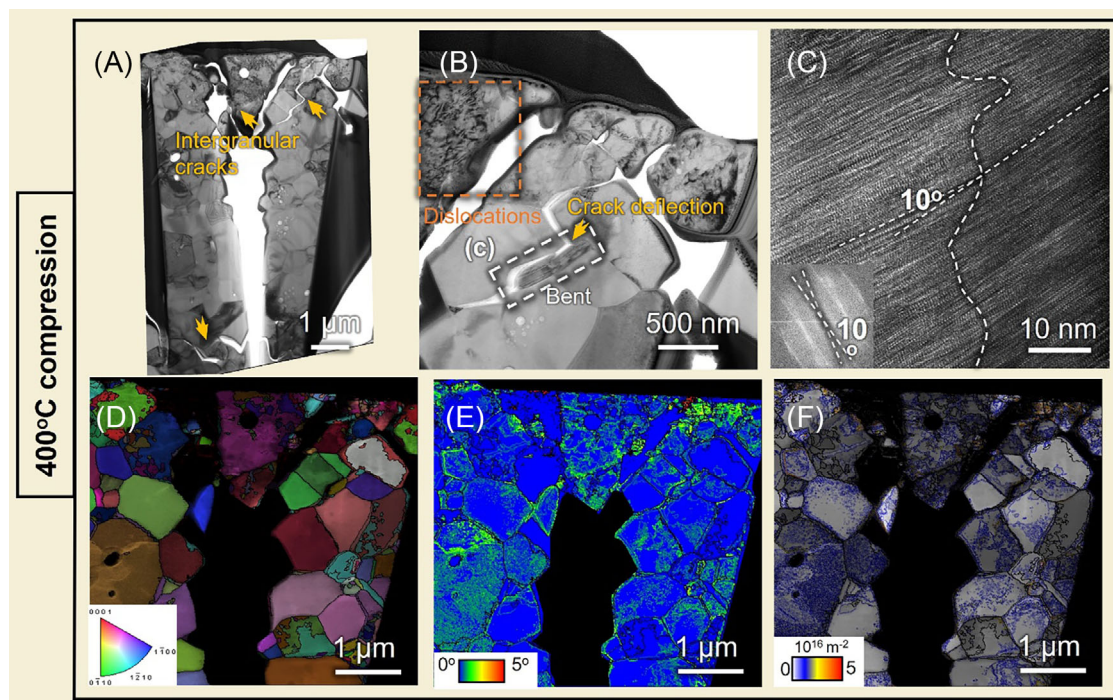


**FIGURE 5** The post-mortem transmission electron microscopy (TEM) analyses of defect formation in the spark plasma sintering (SPS)  $\text{Al}_2\text{O}_3$  micropillar after 400°C compression. (A) A bright-field (BF) TEM micrograph showing some intergranular cracks formed and a giant crack propagated downwards through the entire pillar. (B) BF TEM image of some grains in the upper deformed region shows the presence of dislocations, and a defective grain with a high aspect ratio was bent near one intergranular crack. (C) High-resolution TEM image of the bent defective grain shows a low angle boundary of 10° formation in the interface. (D) The inverse pole figure (IPF) map indicates the mostly equiaxed polycrystalline grains after deformation. (E) The kernel average misorientation (KAM) map shows that the high degree of misorientation was only concentrated within the grains near the fractured top surface, or along the cracks. (F) The geometrically necessary dislocation (GND) map correlates well with the KAM map showing limited dislocation activities.

monotonically when temperature rises. The maximum strain where the pillar fractured decreases slightly from 3.5% at RT to 2.8% at 400°C, followed by a substantial increment to 10.6% when tested at 740°C.

## 4 | DISCUSSION

### 4.1 | Microstructure characteristics of SPS $\text{Al}_2\text{O}_3$

SPS is one of the most efficient consolidation methods to fully compact  $\text{Al}_2\text{O}_3$  at a lower sintering temperature with shorter sintering time than conventional sintering. The microstructures of the SPS specimens can be tuned by adjusting processing parameters including the sintering temperature, heating rate, sintering dwell time, and pressure.<sup>39</sup> Debate exists under the homogeneity of grain size distribution by using SPS. Wang et al. found that the microstructure near edge was denser than the interior for a short holding time of 10 min, suggesting the powder was sintered by heat from the surrounding graphite die.<sup>40</sup> In our study, no obvious grain size difference was visualized

across the sample in the radial direction, where a homogeneous microstructure was achieved with an average grain size of 420 nm as shown in Figure 1. The main reason leading to the previously reported inhomogeneity could be the starting powder size, where the coarse powder with an average particle size of 3.46  $\mu\text{m}$  were used.<sup>40</sup> In comparison, a fine powder with a particle size of 135 nm was utilized in our study. It has been suggested that apart from Joule heating provided by the mold, electric discharge along with an enhanced GB diffusion from the electric field also stimulates the densification and growth of the interior particles, leading to a homogeneous microstructure.<sup>16</sup> Since the discharge mainly arises from the powder-powder contacts at the early stage of sintering, fine particles containing a large specific surface area could generate sufficiently large discharge to promote densification and grain growth, achieving a homogeneous microstructure.

It is interesting to point out that some grains contain a high density of SFs.<sup>5,40,16</sup> The graphite paper separating the powders from the graphite die created a carbon-enriched environment during SPS under vacuum, and abundant oxygen vacancies were potentially created.<sup>10,41</sup> It has been shown that the formation of extended defects includ-

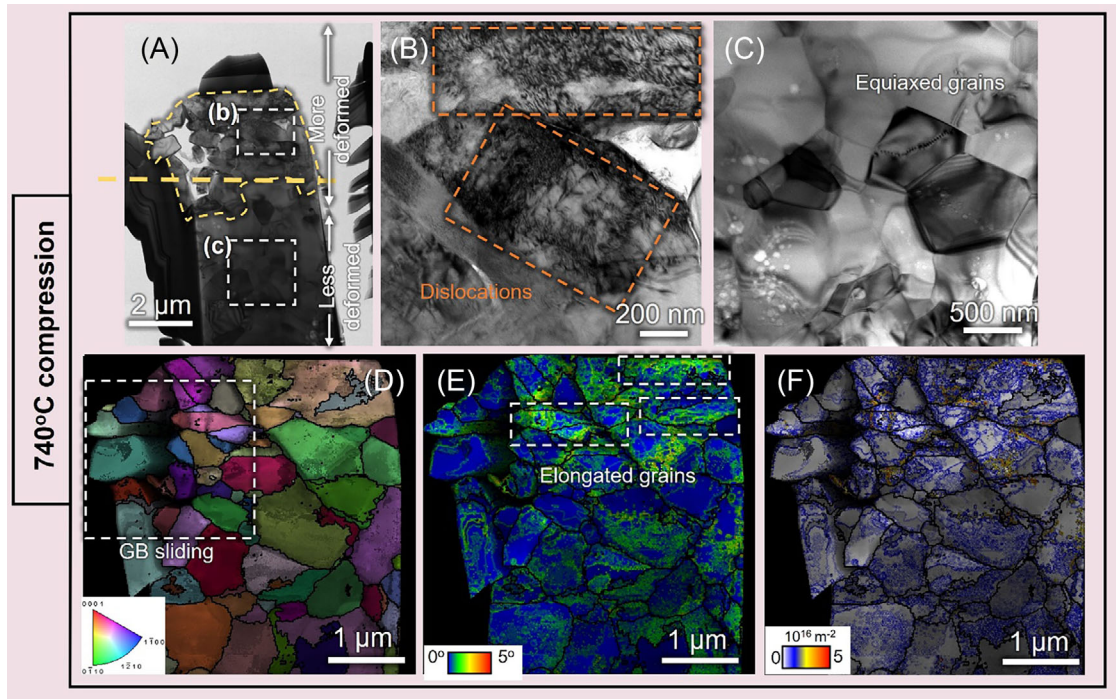


**FIGURE 6** Transmission electron microscopy (TEM) analyses of an  $\text{Al}_2\text{O}_3$  micropillar deformed at  $740^\circ\text{C}$ . (A) A bright-field (BF) TEM micrograph showing obvious dilation of the pillar top. (B) BF TEM image of some grains in the upper deformed region shows a high density of dislocations. (C) BF TEM image of grains in the less deformed region shows the equiaxed grain morphology. (D) The inverse pole figure (IPF) map indicates the polycrystalline feature. Grain separation and cracks formed near the peripheral region. (E) The kernel average misorientation (KAM) map shows a high degree of misorientation within the elongated grains near the pillar top. (F) The geometrically necessary dislocation (GND) map shows evident dislocations were formed within the deformed micropillar.

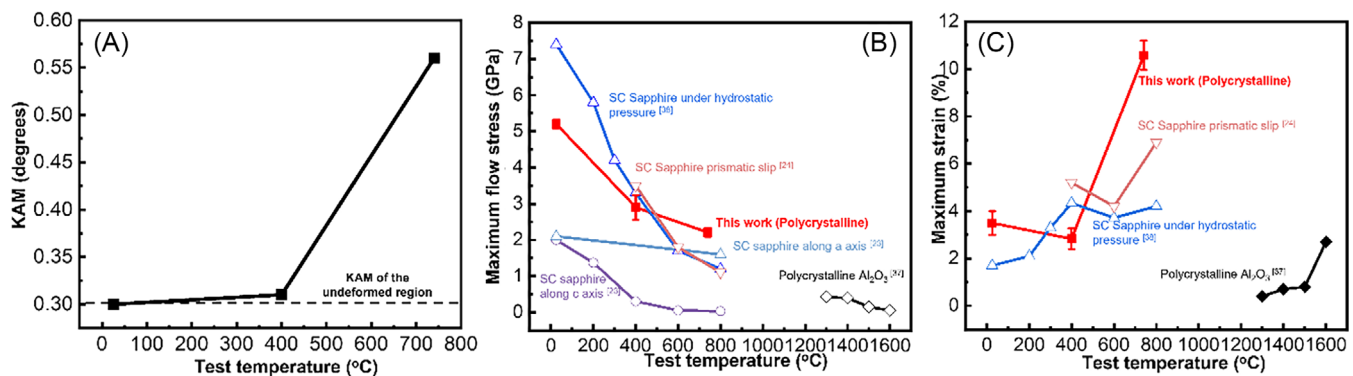


**FIGURE 7** (A) Evolutions of kernel average misorientation (KAM) misorientation angle across entire deformed pillar as a function of test temperature. (B, C) The variation of maximum flow stress and maximum strain with test temperatures from this work and literature data.<sup>23,24,37,38</sup>

ing SFs correlates to the coalescence of charged point defects.<sup>42–45</sup> As many ceramics exhibit negative temperature coefficients of electrical resistance, the impact of electric current on densification extends beyond Joule heating. When the sample temperature is sufficiently high for the electric current to flow through the sample, the current exerts a non-thermal influence directly affecting mass transport through mechanisms such as electroplasticity and electromigration, which potentially leads to

the formation of SFs through the coalescence of charged species.<sup>46</sup>

## 4.2 | Temperature-dependent evolution of deformability in SPS $\text{Al}_2\text{O}_3$

For pillars tested at RT, the catastrophic failure happened immediately after the crack initiation. A mixture of

transgranular and intergranular cracking was visualized, as shown in Figure 3A,B. Interestingly, while the intergranular cracks were distributed throughout the entire pillar, a relatively smooth grain morphology along with some grain fragments was obvious near the pillar top, corresponding to the transgranular fracture mode. The stress concentration near the pillar top drives the growth and coalescence of multiple microcracks within the grain and leads to grain fragmentation.<sup>47</sup> Meanwhile, some intragranular pores were trapped during the sintering process due to high GB mobility. These intragranular pores acted as the weak points for cracks to pass through, leading to transgranular cracking.<sup>48</sup> Moreover, the KAM map and GND map indicate few dislocation activities during the brittle fracture of SPS Al<sub>2</sub>O<sub>3</sub> at RT.

For pillars tested at 400°C and beyond, GBs are weakened due to the decrease of GB cohesive strength, manifested by a significant reduction of crack nucleation stress from 5 GPa at RT to 3 GPa at 400°C. The longitudinal cracks propagated slowly along GBs (Figure 2G), forming the wavy pathway. The crack propagation evolves from primarily transgranular cracking at RT to intergranular cracking at elevated temperatures. As the fracture toughness can be improved by the crack deflection, the presence of intergranular fracture with an increasing crack length gives rise to improved deformability by grain refinement. It was reported that the intergranular cracking may occur due to solute segregation along GB, crystallographic orientation, nanovoids coalescence at the GB, impurities, and localized tensile stress.<sup>49–51</sup> Interatomic bonding and grain boundary strength become weaker, and atomic diffusion is enhanced for most ceramics at elevated temperatures. For the SPS specimens, since the reduced atmosphere created by the carbon-enriched vacuum sintering process could induce abundant point defects, a high density of oxygen vacancies could present along GBs due to the high diffusivity at elevated temperatures.<sup>52</sup> Hence, intergranular cracking may mainly arise from the weakened interatomic bonding along the GBs upon compression. When subjected to compression, these weaker points along the GBs (observed in Figure 1B) provide a favorable route for crack propagation.<sup>53,54</sup> Furthermore, upon uniaxial compression, the dilation of the pillar top (shown in Figure 5A,D) may generate localized tensile and shear stress at GBs. Consequently, the cracks tend to preferentially advance through these GBs that exhibit the least cleavage energy, resulting in the formation of intergranular cracks.<sup>31</sup> Besides the stress-induced cracks along GBs, it is interesting to note that when one crack passed through the aforementioned elongated defective grain, an interface with a misorientation angle of 10° formed, as shown in Figure 5B,C. This bending phenomenon can accommodate the large strain gradient induced by severe plastic

deformation.<sup>55</sup> As shown in the KAM map in Figure 5E, a high degree of misorientation was only concentrated within the grains near the fractured regions or along the cracks. It is interesting to note that the KAM value in the pillar deformed at 400°C is similar to that in the RT-deformed pillar, implying that the dislocation activity is limited at such a test temperature (Figure 7B). The limited plastic strain was carried mainly by microcracking and occasionally by grain bending.<sup>56</sup>

For the pillars tested at 740°C, the brittle failure diminished where much less cracking was present compared to the ones deformed below 400°C. Most cracks reside on the pillar surface (Figure 3F), resolving the grain morphology. Most cracks initiated from the surface barely penetrated through the pillar interior, as shown in Figure 6A. Two factors may play a vital role. It is possible that with less formation energy of point defects near the surface compared to the bulk interior, more oxygen vacancies would nucleate and coalesce, which formed nanovoids towards GBs and resulted in stress concentration.<sup>54,57</sup> In this case, GBs with more nanovoids near the pillar surface resulted in less cohesive strength and experienced more cracking. Secondly, internal grains were confined by neighboring grains and had less degree of freedom. As a consequence, the surface grains exhibited a higher tendency to bow outwards, leading to a higher occurrence of cracks.<sup>53</sup> Grains in the less deformed region near the bottom half were equiaxed, as shown in Figure 6C. It is worth noting that the grains in the pillar interior are elongated in the heavily deformed region near the pillar top, whereas they appear more equiaxed near the pillar surface region, as shown in Figure 6D,E. GB sliding accommodated by diffusion may be prominent near the peripheral region with less dislocation motion.<sup>58</sup> The strain energy exerted on the pillar surface can be accommodated by grain boundary sliding, primarily due to the absence of neighboring grains confining the sliding process. Consequently, before reaching the stress level required for dislocation motion, the strain energy is effectively released through the sliding mechanism. The local grain separation induced by GB sliding and rotation could not be filled by mass transport at 740°C for Al<sub>2</sub>O<sub>3</sub>. For the pillar interior, drastic dislocation activities were observed in the KAM map, as shown in Figure 6E. This finding proves that the dislocation glide and climb contributed to the inelastic deformation, evidenced by the elongated grains in the heavily deformed region. A similar phenomenon has been reported in ZnO systems.<sup>53,59,60</sup> Most GNDs concentrated in the vicinity of cavities and within elongated grains, indicating more GNDs formed to impede the crack nucleation and adapt to the strain gradient within the pillar.<sup>56</sup>

Figure 7A illustrates the evolution of critical strain for crack nucleation in Al<sub>2</sub>O<sub>3</sub> micropillars as a function of

test temperature. The evident decrease of critical strain from RT to 400°C is mainly attributed to the transition of the failure mode from transgranular to intergranular cracking. With the decrease of GB cohesive strength at elevated temperatures, intergranular cracks initiated at lower strain compared to the transgranular ones. Meanwhile, below 400°C, the KAM values are similar to the ones in the undeformed region, implying the test temperature is not sufficiently high to nucleate and activate dislocations. Due to the absence of dislocation activity at 400°C, the limited deformability mainly arises from the microcrack nucleation and crack deflection. In comparison, the KAM values increase drastically from 400 to 740°C, indicating substantial dislocation activities at such a temperature. Grain elongation was observed, and the strain was accommodated by dislocation glide and climb in pillars deformed at 740°C. Previous studies on bulk Al<sub>2</sub>O<sub>3</sub> suggest the BDTT is 1350°C.<sup>29,30</sup> The current study suggests that the BDTT for SPS Al<sub>2</sub>O<sub>3</sub> has reduced significantly to 740°C subjected to uniaxial compression. The prominent improvement in deformability arises from several factors. First, the SPS Al<sub>2</sub>O<sub>3</sub> contains preexisting dislocations. The dislocations may become mobile during deformation at elevated temperatures, and thus significantly improve the plasticity of Al<sub>2</sub>O<sub>3</sub> at 740°C.<sup>61</sup> Similar phenomenon has been shown previously in flash-sintered TiO<sub>2</sub>, where significant plasticity was carried by a high density of preexisting defects during deformation.<sup>62</sup> The preexisting dislocations in FS TiO<sub>2</sub> enable to skip the dislocation nucleation process, the stress of which is typically much greater than fracture stress, and thus promote plasticity. It was also reported that FS Al<sub>2</sub>O<sub>3</sub> with a high density of preexisting defects could show an improved fracture toughness at RT.<sup>5</sup> Second, the submicron grain size has enabled GB sliding at relatively low temperatures, and thus enabling deformability.<sup>63</sup> Third, there may also be an extrinsic size effect arising from the pillar dimensions with an increased surface-to-volume ratio.<sup>21</sup> Previous studies conducted on Si or GaAs demonstrate a reduction of BDTT as the pillar diameter decreased.<sup>32,64</sup> Furthermore, the current micropillars contain small nanopores, with pore size on the order of tens of nm, and thus alleviate GB cracking typically observed in conventionally sintered Al<sub>2</sub>O<sub>3</sub> with large GB voids in large grains. Figure 7B compares flow stresses between polycrystalline and SC Al<sub>2</sub>O<sub>3</sub> under compression. When compressed along the c-axis, SC Al<sub>2</sub>O<sub>3</sub> exhibits prominent softening at higher test temperatures compared to the insensitive variation of flow stress when deformed along a-axis orientation. All SC Al<sub>2</sub>O<sub>3</sub> exhibited limited strength (< 2 GPa) at 600–800°C. In comparison, the flow stress of SPS Al<sub>2</sub>O<sub>3</sub> retains high strength (above 2 GPa) at 740°C, indicating that SPS Al<sub>2</sub>O<sub>3</sub> remains strong at high test temperatures, a trib-

ute necessary for high-temperature structural applications. Furthermore, as shown in Figure 7C, the maximum strain in SPS Al<sub>2</sub>O<sub>3</sub> appears to be much greater than all other data sets for Al<sub>2</sub>O<sub>3</sub> reported in the literature. The combinations of high flow stress and substantial plasticity in SPS Al<sub>2</sub>O<sub>3</sub> enabled by small grain size, dislocations and grain boundary sliding, may bring more structural applications for fine-grained ceramics with preexisting dislocations.

## 5 | CONCLUSION

The temperature-dependent study of SPS Al<sub>2</sub>O<sub>3</sub> was performed by in situ micropillar compression technique at elevated temperatures up to 740°C. At RT, the SPS Al<sub>2</sub>O<sub>3</sub> displayed a brittle failure, characterized by mixed transgranular and intergranular cracking. As the temperature increased to 400°C, a significant strength reduction to 3 GPa was observed, accompanied by a transition to the intergranular cracking mode. Surprisingly, a brittle-to-ductile transition fracture mode was evident at 740°C, occurring at a much lower temperature than the reported 1300°C in conventionally prepared polycrystalline Al<sub>2</sub>O<sub>3</sub>. The enhanced deformability results from the dislocation activity with grain boundary sliding. This study provides insights into the deformation mechanisms of SPS Al<sub>2</sub>O<sub>3</sub> under uniaxial compression under elevated temperatures at the microscale.

## ACKNOWLEDGMENTS

The work is supported by the U.S. Office of Naval Research (Contract Nos. N00014-17-1-2087 and N00014-22-1-2160 for sintering effort and N00014-20-1-2043 for TEM). The ASTAR crystal orientation system in the TEM microscope is supported by ONR-DURIP DURIP project number N00014-20-1-2659. We would like to acknowledge access to the Life Science Microscopy Facility and the microscopy center of the School of Materials Engineering at Purdue University.

## ORCID

Chao Shen  <https://orcid.org/0000-0003-0803-6318>

Haiyan Wang  <https://orcid.org/0000-0002-7397-1209>

Xinghang Zhang  <https://orcid.org/0000-0002-8380-8667>

## REFERENCES

- Pavlacka RJ, Messing GL. Processing and mechanical response of highly textured Al<sub>2</sub>O<sub>3</sub>. *J Eur Ceram Soc.* 2010;30:2917–25. <https://doi.org/10.1016/j.jeurceramsoc.2010.02.009>
- Jiang D, Hulbert DM, Anselmi-Tamburini U, Ng T, Land D, Mukherjee AK. Optically transparent polycrystalline Al<sub>2</sub>O<sub>3</sub> pro-

- duced by spark plasma sintering. *J Am Ceram Soc.* 2008;91:151–54. <https://doi.org/10.1111/j.1551-2916.2007.02086.x>
3. Kermani M, Dong J, Biesuz M, Linx Y, Deng H, Sglavo VM, et al. Ultrafast high-temperature sintering (UHS) of fine grained  $\alpha$ -Al<sub>2</sub>O<sub>3</sub>. *J Eur Ceram Soc.* 2021;41:6626–33. <https://doi.org/10.1016/J.JEURCERAMSOC.2021.05.056>
  4. Jia ZH, Tang XU, Chen DG, Wu JB, Liu QX. Magnetic properties and high thermal conductivity of Al<sub>2</sub>O<sub>3</sub> ceramics prepared by spark plasma sintering. *Adv Mat Res.* 2013;750-752:512–16. <https://doi.org/10.4028/www.scientific.net/AMR.750-752.512>
  5. Shen C, Niu T, Yang B, Cho J, Shang Z, Sun T, et al. Micromechanical properties and microstructures of AC and DC flash-sintered alumina. *Mater Sci Eng A.* 2023;866:144631. <https://doi.org/10.1016/J.MSEA.2023.144631>
  6. Rahaman MN. *Ceramic processing and sintering*. 2nd ed. Boca Raton, FL: CRC Press; 2017.
  7. Guillon O, Gonzalez-Julian J, Dargatz B, Kessel T, Schierning G, Räthel J, et al. Field-assisted sintering technology/spark plasma sintering: mechanisms, materials, and technology developments. *Adv Eng Mater.* 2014;16:830–49. <https://doi.org/10.1002/ADEM.201300409>
  8. Hu ZY, Zhang ZH, Cheng XW, Wang FC, Zhang YF, Li SL. A review of multi-physical fields induced phenomena and effects in spark plasma sintering: fundamentals and applications. *Mater Des.* 2020;191:108662. <https://doi.org/10.1016/J.MATDES.2020.108662>
  9. Munir ZA, Anselmi-Tamburini U, Ohyanagi M. The effect of electric field and pressure on the synthesis and consolidation of materials: a review of the spark plasma sintering method. *J Mater Sci.* 2006;41:763–77. <https://doi.org/10.1007/s10853-006-6555-2>
  10. Demuyneck M, Erauw JP, Van der Biest O, Delannay F, Cambier F. Densification of alumina by SPS and HP: a comparative study. *J Eur Ceram Soc.* 2012;32:1957–64. <https://doi.org/10.1016/j.jeurceramsoc.2011.10.031>
  11. Casellas D, Nagl MM, Llanes L, Anglada M. Fracture toughness of alumina and ZTA ceramics: microstructural coarsening effects. *J Mater Process Technol.* 2003;143-144:148–52. [https://doi.org/10.1016/S0924-0136\(03\)00396-0](https://doi.org/10.1016/S0924-0136(03)00396-0)
  12. Zhang ZH, Liu ZF, Lu JF, Shen XB, Wang FC, Wang YD. The sintering mechanism in spark plasma sintering—proof of the occurrence of spark discharge. *Scr Mater.* 2014;81:56–59. <https://doi.org/10.1016/J.SCRIPTAMAT.2014.03.011>
  13. Hulbert DM, Anders A, Andersson J, Lavernia EJ, Mukherjee AK. A discussion on the absence of plasma in spark plasma sintering. *Scr Mater.* 2009;60:835–38. <https://doi.org/10.1016/J.SCRIPTAMAT.2008.12.059>
  14. Cavaliere P, Sadeghi B, Shabani A. Spark plasma sintering: process fundamentals. In: Cavaliere P, editor. *Spark plasma sintering of materials*. Cham: Springer; 2019;3–20. [https://doi.org/10.1007/978-3-030-05327-7\\_1](https://doi.org/10.1007/978-3-030-05327-7_1)
  15. Nygren M, Shen Z. On the preparation of bio-, nano- and structural ceramics and composites by spark plasma sintering. *Solid State Sci.* 2003;5:125–31. [https://doi.org/10.1016/S1293-2558\(02\)00086-9](https://doi.org/10.1016/S1293-2558(02)00086-9)
  16. Shen Z, Johnsson M, Zhao Z, Nygren M. Spark plasma sintering of alumina. *J Am Ceram Soc.* 2002;85:1921–27. <https://doi.org/10.1111/j.1151-2916.2002.tb00381.x>
  17. Stanciu LA, Kodash VY, Groza JR. Effects of heating rate on densification and grain growth during field-assisted sintering of  $\alpha$ -Al<sub>2</sub>O<sub>3</sub> and MoSi<sub>2</sub> powders. *Metall Mater Trans A Phys Metall Mater Sci.* 2001;32:2633–38. <https://doi.org/10.1007/s11661-001-0053-6>
  18. Zhou Y, Hirao K, Yamauchi Y, Kanzaki S. Densification and grain growth in pulse electric current sintering of alumina. *J Eur Ceram Soc.* 2004;24:3465–70. <https://doi.org/10.1016/j.jeurceramsoc.2003.10.013>
  19. Kim BN, Hiraga K, Morita K, Yoshida H. Effects of heating rate on microstructure and transparency of spark-plasma-sintered alumina. *J Eur Ceram Soc.* 2009;29:323–27. <https://doi.org/10.1016/j.jeurceramsoc.2008.03.015>
  20. Ratzker B, Wagner A, Sokol M, Kalabukhov S, Frage N. Stress-enhanced dynamic grain growth during high-pressure spark plasma sintering of alumina. *Acta Mater.* 2019;164:390–99. <https://doi.org/10.1016/j.actamat.2018.11.001>
  21. Montagne A, Pathak S, Maeder X, Michler J. Plasticity and fracture of sapphire at room temperature: load-controlled microcompression of four different orientations. *Ceram Int.* 2014;40:2083–90. <https://doi.org/10.1016/J.CERAMINT.2013.07.121>
  22. Heuer AH. Deformation twinning in corundum. *J Theor Exp Appl Phys.* 1966;13:379–93. <https://doi.org/10.1080/14786436608212616>
  23. Scott WD, Orr KK. Rhombohedral twinning in alumina. *J Am Ceram Soc.* 1983;66:27–32. <https://doi.org/10.1111/J.1151-2916.1983.TB09962.X>
  24. Lagerlöf KPD, Heuer AH, Castaing J, Rivière JP, Mitchell TE. Slip and twinning in sapphire ( $\alpha$ -Al<sub>2</sub>O<sub>3</sub>). *J Am Ceram Soc.* 1994;77:385–97. <https://doi.org/10.1111/J.1151-2916.1994.TB07006.X>
  25. Trabadelo V, Pathak S, Saeidi F, Parlinska-Wojtan M, Wasmer K. Nanoindentation deformation and cracking in sapphire. *Ceram Int.* 2019;45:9835–45. <https://doi.org/10.1016/j.ceramint.2019.02.022>
  26. Castaing J, Muñoz A, Gomez Garcia D, Dominguez Rodriguez A. Basal slip in sapphire ( $\alpha$ -Al<sub>2</sub>O<sub>3</sub>). *Mate Sci Eng A.* 1997;233:121–25. [https://doi.org/10.1016/s0921-5093\(97\)00056-7](https://doi.org/10.1016/s0921-5093(97)00056-7)
  27. Castaing J, He A, Lagerlöf KPD, Heuer AH. Deformation of sapphire ( $\alpha$ -Al<sub>2</sub>O<sub>3</sub>) by basal slip and basal twinning below 700°C. *Philos Mag.* 2004;84:1113–25. <https://doi.org/10.1080/14786430310001613183>
  28. Castillo-Rodríguez M, Muñoz A, Castaing J, Veysière P, Domínguez-Rodríguez A. Basal slip latent hardening by prism plane slip dislocations in sapphire ( $\alpha$ -Al<sub>2</sub>O<sub>3</sub>). *Acta Mater.* 2010;58:5610–19. <https://doi.org/10.1016/j.actamat.2010.06.033>
  29. Passmore E, Moschetti A, Vasilos T. The brittle-ductile transition in polycrystalline aluminium oxide. *Philos Mag.* 1966;13:1157–62. <https://doi.org/10.1080/14786436608213531>
  30. by Spriggs RM, Mitchell JB. Mechanical properties of pure, dense aluminum oxide as a function of temperature and grain size. *J Am Ceram Soc.* 1964;47:323–27.
  31. Heuer AH, Cannon RM, Tighe NJ. Plastic deformation in fine-grain ceramics. In: Burke JJ, Reed NL, Weiss V, editors. *Ultrafine-grain ceramics*. Boston, MA: Springer; 1970;339–65.
  32. Östlund F, Rzepiejewska-Malyska K, Leifer K, Hale LM, Tang Y, Ballarini R, et al. Brittle-to-ductile transition in uniax-

- ial compression of silicon pillars at room temperature. *Adv Funct Mater.* 2009;19:2439–44. <https://doi.org/10.1002/ADFM.200900418>
33. Wei B, Wu W, Xie D, Nastasi M, Wang J. Strength, plasticity, thermal stability and strain rate sensitivity of nanograined nickel with amorphous ceramic grain boundaries. *Acta Mater.* 2021;212:116918. <https://doi.org/10.1016/J.ACTAMAT.2021.116918>
  34. Korte S, Clegg WJ. Micropillar compression of ceramics at elevated temperatures. *Scr Mater.* 2009;60:807–10. <https://doi.org/10.1016/j.scriptamat.2009.01.029>
  35. Camposilvan E, Anglada M. Size and plasticity effects in zirconia micropillars compression. *Acta Mater.* 2016;103:882–92. <https://doi.org/10.1016/j.actamat.2015.10.047>
  36. Maiti K, Sil A. Relationship between fracture toughness characteristics and morphology of sintered  $\text{Al}_2\text{O}_3$  ceramics. *Ceram Int.* 2010;36:2337–44. <https://doi.org/10.1016/j.ceramint.2010.07.031>
  37. Ishihara S, Furushiro N, Hori S. High temperature deformation of fine grained high purity alumina. *Mater Trans.* 1999;40:1005–10. <https://doi.org/10.2320/MATERTRANS1989.40.1005>
  38. Castaing J, Cadoz J, Kirby SH. Prismatic slip of  $\text{Al}_2\text{O}_3$  single crystals below 1000°C in compression under hydrostatic pressure. *J Am Ceram Soc.* 1981;64:504–11. <https://doi.org/10.1111/J.1151-2916.1981.TB10314.X>
  39. Santanach JG, Weibel A, Estourns C, Yang Q, Laurent C, Peigney A. Spark plasma sintering of alumina: study of parameters, formal sintering analysis and hypotheses on the mechanism(s) involved in densification and grain growth. *Acta Mater.* 2011;59:1400–1408. <https://doi.org/10.1016/j.actamat.2010.11.002>
  40. Wang SW, Chen LD, Hirai T. Densification of  $\text{Al}_2\text{O}_3$  powder using spark plasma sintering. *J Mater Res.* 2000;15:982–87. <https://doi.org/10.1557/JMR.2000.0140>
  41. Cho J, Li J, Li Q, Ding J, Wang H, Xue S, et al. In-situ high temperature micromechanical testing of ultrafine grained yttria-stabilized zirconia processed by spark plasma sintering. *Acta Mater.* 2018;155:128–37. <https://doi.org/10.1016/j.actamat.2018.05.062>
  42. Steil MC, Marinha D, Aman Y, Gomes JRC, Kleitz M. From conventional ac flash-sintering of YSZ to hyper-flash and double flash. *J Eur Ceram Soc.* 2013;33:2093–101. <https://doi.org/10.1016/j.jeurceramsoc.2013.03.019>
  43. Dang Y, West AR. Oxygen stoichiometry, chemical expansion or contraction, and electrical properties of rutile,  $\text{TiO}_{2\pm\delta}$  ceramics. *J Am Ceram Soc.* 2018;102:251–59. <https://doi.org/10.1111/jace.15889>
  44. Santara B. Microscopic origin of lattice contraction and expansion in undoped rutile  $\text{TiO}_2$  nanostructures. *Phys D Appl Phys.* 2014;47 215302. <https://doi.org/10.1088/0022-3727/47/21/215302>
  45. Yang B, Shang Z, Li J, Phuah XL, Cho J, Wang H, et al. Effects of electric field on microstructure evolution and defect formation in flash-sintered  $\text{TiO}_2$ . *J Eur Ceram Soc.* 2022;42:6040–47. <https://doi.org/10.1016/j.jeurceramsoc.2022.06.009>
  46. Olevsky EA, Kandukuri S, Froyen L. Consolidation enhancement in spark-plasma sintering: impact of high heating rates. *J Appl Phys.* 2007;102:1–12. <https://doi.org/10.1063/1.2822189>
  47. Ohara T, Yamada T. Fatigue crack growth from indentation flaw in ceramics. *Int J Fract.* 1988;37:47–59.
  48. Roberts JTA, Ueda Y. Porosity on deformation and fracture of UO. *J Am Ceram Soc.* 1972;55:117–24. <https://doi.org/10.1111/j.1151-2916.1972.tb11233.x>
  49. Emdadi A, Zaeem MA. Phase-field modeling of crack propagation in polycrystalline materials. *Comput Mater Sci.* 2020;86:110057. <https://doi.org/10.1016/j.commatsci.2020.110057>
  50. Liang FL, Laird C. Control of intergranular fatigue cracking by slip homogeneity in copper I: effect of grain size. *Mater Sci Eng A.* 1989;117:95–102. [https://doi.org/10.1016/0921-5093\(89\)90090-7](https://doi.org/10.1016/0921-5093(89)90090-7)
  51. Wang Z, Li P. Dynamic failure and fracture mechanism in alumina ceramics: experimental observations and finite element modelling. *Ceram Int.* 2015;41:12763–72. <https://doi.org/10.1016/j.ceramint.2015.06.110>
  52. Liang J, Zhao X, Sun J, Ren L, Liao R, Yang L, et al. Enhanced electrical properties of ZnO varistor ceramics by spark plasma sintering: role of annealing. *Ceram Int.* 2020;46:15076–83. <https://doi.org/10.1016/j.ceramint.2020.03.042>
  53. Cho J, Phuah XL, Li J, Shang Z, Wang H, Charalambous H, et al. Temperature effect on mechanical response of flash-sintered ZnO by in-situ compression tests. *Acta Mater.* 2020;200:699–709. <https://doi.org/10.1016/J.ACTAMAT.2020.09.029>
  54. Espinosa HD, Bernal RA, Minary-Jolandan M, Espinosa HD, Bernal RA, Minary-Jolandan M. A review of mechanical and electromechanical properties of piezoelectric nanowires. *Adv Mater.* 2012;24:4656–75. <https://doi.org/10.1002/ADMA.201104810>
  55. Becher PF. Microstructural design of toughened ceramics. *J Eur Ceram Soc.* 1991;74:255–69. <https://doi.org/10.1111/j.1151-2916.1991.tb06872.x>
  56. Zhu C, Harrington T, Livescu V, Gray Iii GT, Vecchio KS. Determination of geometrically necessary dislocations in large shear strain localization in aluminum. *Acta Mater.* 2016;118:383–94. <https://doi.org/10.1016/j.actamat.2016.07.051>
  57. Deng B, Luisa Da Rosa A, Frauenheim T, Xiao JP, Shi XQ, Zhang RQ, et al. Oxygen vacancy diffusion in bare ZnO nanowires. *Nanoscale.* 2014;6:11882–86. <https://doi.org/10.1039/C4NR03582H>
  58. Ashby MF, Verrall RA. Diffusion-accommodated flow and superplasticity. *Acta Metallurgica.* 1973;21:149–63.
  59. John MJM, Wachtman B, Cannon WR. Mechanical properties of ceramics. 2nd ed. Hoboken, NJ: Wiley; 2009.
  60. Courtney TH. Mechanical behavior of materials. 2nd ed. New York, NY: McGraw Hill Education; 2017.
  61. Porz L. 60 years of dislocations in ceramics: a conceptual framework for dislocation mechanics in ceramics. *Int J Ceram Eng Sci.* 2022;4:214–39. <https://doi.org/10.1002/ces2.10150>
  62. Li J, Cho J, Ding J, Charalambous H, Xue S, Wang H, et al. Nanoscale stacking fault–assisted room temperature plasticity in flash-sintered  $\text{TiO}_2$ . *Sci Adv.* 2019;5:eaaw5519. [https://doi.org/10.1126/SCIADV.AAW5519/SUPPL\\_FILE/AAW5519\\_SM.PDF](https://doi.org/10.1126/SCIADV.AAW5519/SUPPL_FILE/AAW5519_SM.PDF)
  63. Sergueeva AV, Mara NA, Mukherjee AK. Grain boundary sliding in nanomaterials at elevated temperatures. *J Mater Sci.* 2007;42:1433–38. <https://doi.org/10.1007/S10853-006-0697-0/FIGURES/4>
  64. Östlund F, Howie PR, Ghisleni R, Korte S, Leifer K, Clegg WJ, et al. Ductile-brittle transition in micropillar compression of

GaAs at room temperature. *Philos Mag.* 2011;91:1190–99. <https://doi.org/10.1080/14786435.2010.509286>

## SUPPORTING INFORMATION

Additional supporting information can be found online in the Supporting Information section at the end of this article.

**How to cite this article:** Shen C, Niu T, Cho J, Sun T, Shang A, Zhang Y, et al. In situ studies on temperature-dependent deformation mechanisms of Al<sub>2</sub>O<sub>3</sub> prepared by spark plasma sintering. *J Am Ceram Soc.* 2024;1–12.

<https://doi.org/10.1111/jace.19964>